Hyperspectral Imaging of In-Site Stained Glasses: Illumination Variation Compensation Using Two Perpendicular Scans

Suzan Joseph Kessy[1]   Takuya Funatomi[1]   Kazuya Kitano[1]   Yuki Fujimura[1]
Guillaume Caron[2,3]   El Mustapha Mouaddib[2]   Yasuhiro Mukaigawa[1]
[1]Nara Institute of Science and Technology   [2]University of Picardie Jules Verne
[3]CNRS-AIST JRL (Joint Robotics Laboratory), IRL

{kessy.suzan_joseph.ks5, funatomi, fujimura.yuki, kitano.kazuya}@is.naist.jp

{mouaddib, guillaume.caron}@u-picardie.fr, mukaigawa@is.naist.jp

Abstract

This paper presents a method for compensating temporal illumination variations in whisk-broom hyperspectral imaging. Whisk-broom imaging scans the scene sequentially, capturing a complete spectrum at each spatial coordinate pixel-by-pixel over time. The scanning process takes time, which is not problematic under constant illumination, but capturing cultural artefacts on-site often involves sunlight as the natural illumination source. While it may be considered beneficial due to its broad spectrum, sunlight fluctuates over time. Thus the resulting hyperspectral image suffers from temporal illumination variation, affecting the observed value and hindering scene analysis. A previous approach proposed using a quick extra single-vertical scan alongside the standard raster (horizontal) scan for compensation. However, it fails when the additional single-vertical scan is performed near or on a black frame. This work aims to overcome this issue by incorporating multiple columns or a full-vertical scan (column scan) to the horizontal scan image (row scan). Furthermore, we introduce a logarithm space and utilise the low-dimensional structures of the illumination and reflectance spectra. Experiments show that the proposed method eliminates the temporal illumination variations in the in-site captured hyperspectral images of stained-glass windows in the historic Amiens Cathedral, France.

1. Introduction

In cultural heritage, digital studies of materials and features have become imperative for acquiring knowledge about cultural artefacts and archaeological objects. Such studies provide historians, scholars, conservators, and archaeologists with efficient tools to enhance their understanding and guide appropriate preservation measures [22].
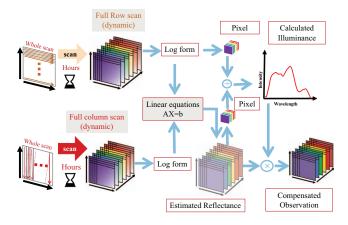

Figure 1: The framework of the proposed method for illumination compensation.

More than traditional RGB information is required to capture and analyse cultural artefacts' subtle variations. Therefore, utilising spectral data, particularly through hyperspectral imaging (HSI), becomes essential. HSI measures a scene's spectral radiance $I(U, V, \lambda)$, collecting three-dimensional information commonly known as a datacube. Unlike RGB cameras that offer information in three channels, HSI provides a much higher level of spectral discrimination capturing data across numerous narrow bands of up to more than 2000 bands [24].

This allows comprehensive analysis and identification of materials or features based on their distinctive spectral signatures [23]. This assists in identifying hidden details, studying pigments and materials, detecting damages or degradation, and guiding appropriate conservation measures even for rendering such cultural heritage artefacts [7]. However, capturing hyperspectral images is challenging.

The datacubes have an extra dimension, that is, the 2D spatial (U, V) and wavelength axis λ, but we use available 2D detector arrays to create the 3D datacube [17]. System designers either measure time-sequential 2D slices of the datacube or divide the datacube into multiple 2D elements that can be recombined into a datacube during post-processing [12]. These approaches are commonly referred to as scanning and snapshot methods. Although the whisk-broom scanning approach is favoured for its superior spectral resolution and flexibility in spatial scanning [11], it scans a scene one pixel at a time, resulting in a time-consuming acquisition process.

Acquiring data from stained glass windows presents challenges due to their transparent nature. Measurement setups must effectively capture transmittance while accommodating the stained glass's size. In outdoor measurements, natural sunlight offers a practical solution, eliminating the need for complex lighting arrangements. However, fluctuations in light conditions and the time-consuming acquisition process introduce temporal illumination variations [1, 21], affecting spectral cubes and hindering scene analysis. This issue persists when measuring the same stained-glass window at different times. Although capturing a reference object under sunlight during scanning helps correct for the variation, it is not feasible inside buildings.

This paper proposes a method to eliminate temporally varying illumination in whisk-broom HSI without requiring a reference object. Specifically, we introduce using two spectral cubes, with one cube scanned perpendicular to the other. Furthermore, linear models are formed by presenting the cubes in spectral logarithm space and leveraging on low-dimensional models to address problem. Quantitative and qualitative evaluations confirm that the proposed model eliminates temporal illumination variations. Consequently, this approach enables the acquisition of a spectral cube with high spectral and spatial resolution, even in natural illumination variations. The specific achievements of this paper are as follows:

1. The paper proposes the use of two spectral images with one cube scanned perpendicular to the other leveraging on the flexibility of whisk-broom imaging system.

2. The utilisation of the logarithm space of the spectral data which allows the formation of linear equations for efficient and analytical solutions.

3. Through quantitative evaluation using a public dataset, our proposed method outperforms a previous state-of-the-art approach.

4. Field experiments on stained-glass windows inside Amiens Cathedral demonstrated the effectiveness and performance of the proposed method.
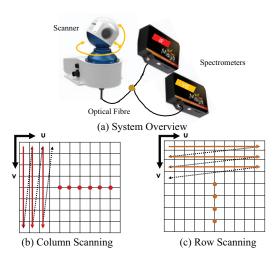

Figure 2: (a) Overview of the imaging system designed in this study. (b) The red arrows illustrate the whisk-broom column-wise scanning to form a column scan image. (c) The orange arrows illustrate the whisk-broom row-wise scanning to form a row-scan image.

2. Related Work

An image is formed through the interaction of illumination spectral power distribution and surface reflectance spectra. Illumination and reflectance spectra separation (IRSS) has been a long-standing problem in computer vision tasks. This separation is crucial because an object's perceived colour relies on the surface spectral reflectance rather than the spectrum of incident illumination [25]. Previous approaches addressing the IRSS problem can be categorised into groups on RGB images and those based on multi or hyperspectral images. In the context of RGB images, a notable work is the gamut mapping algorithm by [10]. It estimates the illuminant based on the limited observable RGB values under a given illuminant. Other approaches include the Max-RGB algorithm, which estimates the light source colour using the maximum response of different colour channels [18]. The Grey-World method [3] assumes that the illuminant colour is the average colour of all image pixels, considering object reflectance to be, on average, grey. While some methods for the IRSS problem rely on image statistics [2, 9]. Regarding spectral data, an initial approach to IRSS by [13] approximated illumination and reflectance spectra as a linear combination of distinct basis spectra. They recovered these spectra using statistical distributions within a space described by finite linear models. Subsequently, [4] improved accuracy by imposing constraints on reflectance and illumination and used simulated annealing to avoid local optima. Additionally, [8] enhanced computational speed by introducing an analytic solution involving logarithms and incorporating an extra re-

Figure 3: Experimental setup: The object is a colour chart of ColorCheckerPassport (X-rite, Inc) under uncontrollable illumination near a window.

gression step for result refinement. Researchers have generalised IRSS-RGB image methods to address the IRSS problem in hyperspectral images. For example, [15] estimated illumination and reflectance spectra based on the dichromatic reflectance model, while [14] introduced a subspace-based model to extract reflectance and shading components as a convex optimisation problem, building upon the assumption of [18]. However, all methods assume constant illumination and do not consider temporally varying environments when capturing hyperspectral images. To address this, [26] proposed a low-rank matrix factorisation approach using singular value decomposition (SVD) to separate illumination and reflectance under general spectral illumination. Additionally, [5] utilised a Conditional Random Field (CRF) model to estimate reflectance under multiple illumination conditions by incorporating spatial information in local patches. However, this approach lacks effective compensation for temporally varying illumination in hyperspectral images acquired using whisk-broom scanning systems. [11] introduced a technique to compensate for the temporal illumination changes in whisk-broom HSI by incorporating an additional single-column scan alongside the raster scan. However, this method relies on the selected column and becomes more prone to errors when the extra scan is performed near or on a black frame.

In contrast, our approach avoids relying on restrictive column selection and employs the full column instead. Specifically, we capture two scans of the scene, with one image (row scan) being scanned perpendicular to the other (column scan).

3. Proposed method

3.1. Image formation model

A hyperspectral image, denoted as $\mathcal{I} \in \mathbb{R}_+^{U \times V \times \lambda}$, captures comprehensive data in a 3D format, including positional and wavelength information. Here, U and V represent the image height and width, respectively, and λ is the number of spectral channels.

Each pixel, referred to as a spectral vector $i_{u,v}$ records a continuous observation value along the wavelength axis. Let $\rho_{u,v}$ and l denote reflectance (or transmittance) at point (u, v) and illumination spectrum respectively. Then spectral vector $i_{u,v}$ can then be presented as:

$$i_{u,v} = \rho_{u,v} \odot l, \tag{1}$$

where $\odot$ is the Hadamard (element-wise) product.

Scanning outdoor scenes with a whisk-broom imaging device is time-consuming [6]. The illumination varies over time due to sunlight fluctuations, making the illumination spectrum a function of time. Thus, Eq. (1) can be written as:

$$i_{u,v} = \rho_{u,v} \odot l(t), \tag{2}$$

where $l(t)$ can be defined at the moment each scan has been performed. t is the time taken to perform a scan. Here, our goal is to recover the hyperspectral image unaffected by these variations.

3.2. Compensation for illumination changes

This study developed whisk-broom imaging device comprises two high spectral-resolution spectrometers and a two-dimensional mechanical scanning head. Figure 2 (a) illustrates the composition of the system. The mechanical scanner head is flexible and scans with a spatial resolution up to $0.01°$ for $360°$ in azimuth direction and $70°$ elevation direction to form a spatially hyperspectral image. In this manner, it can systematically scan the scene row by row (row scanning) or column by column (column wise). For column scan, the scan order is from top to bottom in each column and column by column from left to right, as illustrated by the red arrows in Figure 2 (b). For row scanning, the scan order is from left to right in each row, and row-by-row from top to bottom, as illustrated by the orange arrows in Figure 2 (c).

To simplify the problem, we make the assumption that the variations in illumination are insignificant or constant while scanning a row or column in the respective row or column scan image. Suppose row and column scan images are noted as $i^{\downarrow}$ and $i^{\rightarrow}$ respectively. Thus, spectral vectors can be expressed as:

$$\begin{aligned} i_{u,v}^{\rightarrow} &= \rho_{u,v} \odot l(t_u^{\rightarrow}) \\ i_{u,v}^{\downarrow} &= \rho_{u,v} \odot l(t_v^{\downarrow}), \end{aligned} \tag{3}$$

where $t^{\rightarrow}$ and $t^{\downarrow}$ can be defined as:

$$t^{\rightarrow} \in [t_1^{\rightarrow} \cdots t_U^{\rightarrow}]$$
$$t^{\downarrow} \in \left[t_1^{\downarrow} \cdots t_V^{\downarrow}\right]. \tag{4}$$

3.2.1 Reflectance estimation

Firstly, our proposed method emphasises the separation of illumination and reflectance spectra; we then utilise the estimated reflectance to mitigate the effects of temporal illumination variations. Given that the formulation of the hyperspectral image follows a multiplicative model, as expressed in Eq. (2), we can transform the formulation into logarithmspectral space. By doing so, we can rewrite Eq. (3) as an additive equation in a wavelength-independent format, resulting in a $linear$ representation as:

$$\log i_{u,v}^{\rightarrow} = \log \rho_{u,v} + \log l(t_u^{\rightarrow})$$
$$\log i_{u,v}^{\downarrow} = \log \rho_{u,v} + \log l(t_v^{\downarrow}). \tag{5}$$

Previous studies such as [8, 16] have demonstrated that illumination and reflectance spectra can be assumed to have a low-dimensional spectral property. Building on this, we propose an approximation for the logarithm of the illumination ($\log l$) and reflectance spectra ($\log \rho$) as a linear combination of a limited set of basis spectra as follows:

$$\log l(t_u^{\rightarrow}) \simeq \sum_{i=1}^{m} \epsilon_{u,i}^{\rightarrow} E_i, \tag{6}$$

$$\log l(t_v^{\downarrow}) \simeq \sum_{i=1}^{m} \epsilon_{v,i}^{\downarrow} E_i, \tag{7}$$

$$\log \rho_{u,v} \simeq \sum_{j=1}^{n} \sigma_j S_j, \tag{8}$$

where m, n are the number of illumination and reflectance basis, respectively, and ϵ_i, σ_j are the weighting factor associated with basis spectrum E_i and S_j. Using this low-dimensional approximation, we can rewrite Eq. (5) as:

$$\log i_{u,v}^{\rightarrow} = \sum_{j=1}^{n} \sigma_j S_j + \sum_{i=1}^{m} \epsilon_{u,i}^{\rightarrow} E_i$$
$$\log i_{u,v}^{\downarrow} = \sum_{j=1}^{n} \sigma_j S_j + \sum_{i=1}^{m} \epsilon_{v,i}^{\downarrow} E_i. \tag{9}$$

Furthermore, we can express Eq. (9) in matrix form. Notably, the spatial structure has been embedded into the equation, resulting in the following expression:

$$c = \begin{bmatrix} I_{U \times V} & I_U \otimes 1_V & 0 \\ I_{U \times V} & 0 & 1_U \otimes I_V \end{bmatrix} \begin{bmatrix} \sigma_j & 0 \\ 0 & \epsilon_i^{\rightarrow} \\ 0 & \epsilon_i^{\downarrow} \end{bmatrix} \begin{bmatrix} S_j \\ E_i \end{bmatrix}, \tag{10}$$

where I_N is an an $N \times N$ identity matrix, $\otimes$ is the Kronecker product operator, 1_N is an N-dimensional vector of
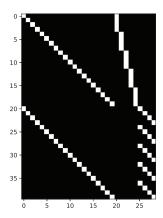

Figure 4: Illustration of the coefficient matrix A under the assumption that the illumination change is constant in every individual row (u) or column scan (v).

ones. In the other hand, c is the observation matrix such that:

$$c = \left[\ \log i_{1,1}^{\rightarrow} \cdots \log i_{U,V}^{\rightarrow} \ | \ \log i_{1,1}^{\downarrow} \cdots \log i_{U,V}^{\downarrow} \ \right]^{\top}. \tag{11}$$

Let $A = \begin{bmatrix} I_{U \times V} & I_U \otimes 1_V & 0 \\ I_{U \times V} & 0 & 1_U \otimes I_V \end{bmatrix}$ represent the vectors of coefficient matrices, $W = \begin{bmatrix} \sigma_j & 0 \\ 0 & \epsilon_i^{\rightarrow} \\ 0 & \epsilon_i^{\downarrow} \end{bmatrix}$ be the weight of the basis matrix, and $B = \begin{bmatrix} S_j \\ E_i \end{bmatrix}$ represent the matrix of the basis vectors. As such, Eq. (10) can simply be represented as:

$$c = AWB. \tag{12}$$

Figure 4 illustrates the coefficient matrix A when $U = 5$ and $V = 4$.

Given that the illumination and reflectance spectra have the low-rank property, we introduce Singular Value Decomposition (SVD) to extract the principal components (or the eigenvectors) from the observation matrix c. Thus given observation c, it can be factorised by SVD to:

$$c = \overline{U} D \overline{V}^{\top} = \sum_{i=1}^{r_x} \overline{u_i} \Sigma_i \overline{v_i}^{\top}, \tag{13}$$

where $\overline{U}$ and $\overline{V}$ are the orthogonal matrices, and D is the diagonal matrix containing the singular values. The left and the right vectors $\overline{u_i}$ and $\overline{v_i}$ are the i-th columns of $\overline{U}$ and $\overline{V}$, respectively; Σ_i is the i-th singular value, and r_x is the rank of c.

By using Eq. (12) and Eq. (13) we form:

$$c = \overline{U} D \overline{V}^{\top} = AWB. \qquad (14)$$

We can further equate:

$$\begin{aligned} \overline{U}D &= AW \\ \overline{V}^{\top} &= B. \end{aligned} \qquad (15)$$

In Eq. (15), the variables $\overline{U}$, D, and A correspond to known values. By representing $\overline{U}D$ as Y, we can derive a linear equation denoted by:

$$Y = AW. \qquad (16)$$

The utilization of logarithm space in the formulation of Eq. (16) introduces the need for careful consideration of negative or small values when solving it to estimate the parameter W. This precaution is essential to preserve mathematical consistency and numerical accuracy, as emphasised by [8]. Furthermore, saturation occurs when a sudden increase in sunlight and the captured scene's radiance exceeds the spectrometer's limited range. Consequently, the pixel intensity becomes clipped at its maximum output value.

To tackle these challenges, our proposed method incorporates intensity filtering. Initially, we establish an *intensity threshold* by defining upper and lower limits. This threshold is vital in filtering undesired data outside the desired range. We then defined the *spectrum filter* and *pixel filter*. For the *spectrum filter*, we exclusively considered spectral channels with intensity values surpassing the upper threshold. It should be noted that we cannot recover the image at the wavelength once the channel is filtered out. For the *pixel filter*, we ensured that the minimum value of the pixels in the *spectrum filter* exceeded the lower limit, given that we do not filter all pixels on a given row or column.

Given A in Eq. (16) is a large sparse and non-invertible matrix, we employed the mean square minimisation approach based on linear regression. This approach proved to be most suitable for determining the optimal values for W. After obtaining $\overline{W}$, we then separated the illumination and reflectance components by multiplying it with the basis matrix B and applying element wise exponential, as shown in Eq. (17). Letting N represent the matrix multiplication $\overline{W}B$, the estimated illumination spectra $\overline{l(t_u^{\rightarrow})}$, $\overline{l(t_v^{\downarrow})}$, and reflectance spectra $\overline{\rho_{u,v}}$ can be represented as:

$$\begin{bmatrix} \overline{l(t_u^{\rightarrow})} \\ \overline{l(t_v^{\downarrow})} \\ \overline{\rho_{u,v}} \end{bmatrix} = e^{\circ N}, \qquad (17)$$

where $\overline{W}$ is the estimated weight matrix and $\{e^{\circ N}\}_{ij} = e^{N_{ij}}$.

Figure 5: Experimental setup: Stained-glass window capture in Cathédrale Notre-Dame d'Amiens.

3.2.2 Compensation

Since the illumination l and reflectance $\rho_{u,v}$ spectra are unknown, the separation problem is non-unique. This is because one can arbitrarily form the spectral vectors $i_{u,v}$ with unknown illumination l and reflectance $\rho_{u,v}$ spectra. Thus, we create a sub-goal to compensate for the illumination variation, we guide the compensation by utilizing a pixel $k_{x,y}$ from the row scan image ($\overrightarrow{i_{u,v}}$) and pixel $j_{x,y}$ from the estimated reflectance ($\overline{\rho_{u,v}}$) where x and y represents the selected row and column. The procedure for compensation is as follows:

1. A pixel, denoted as $k_{x,y}$, was manually selected from the row scan image ($\overrightarrow{i_{u,v}}$).

2. At the same location x, y, a corresponding pixel denoted as $j_{x,y}$ was manually selected from the estimated reflectance ($\overline{\rho_{u,v}}$).

3. For each wavelength, we estimated the illumination amplitude using $k_{x,y}$ and the reflectance $j_{x,y}$.

4. By multiplying this illumination spectrum by the estimated reflectance, we obtain spectral vector $\overline{i_{u,v}}$ which is free from (temporal) variation in the illumination spectra.

Figure 1 summarizes the proposed method.

4. Results and Discussions

A series of experiments were carried out to evaluate the effectiveness and performance of the proposed method, comparing it with the Robust Principal Component Analysis (RPCA) method proposed by [11]. The experimental procedures were as follows: First, a custom imaging system was developed, comprising a scanning head and two one-point spectrometers, as depicted in Figure 2 (a). The spectrometers employed in this system were the Maya2000 Pro models manufactured by Ocean Optics, Inc. These spectrometers offer 2068 channels, the visible range ("VIS")

spectrometer covers a spectral range from $199.50\,\mathrm{nm}$ to $1118.15\,\mathrm{nm}$, and the Infrared ("IR") spectrometer covers a spectral range from $500.81\,\mathrm{nm}$ to $1398.87\,\mathrm{nm}$, with an approximate spectral resolution of $0.5\,\mathrm{nm}$. The RobotEye REHS25, a high-precision scanning device manufactured by Ocular Robotics Ltd., was utilised; it provides a spatial resolution of up to $0.01°$ for $360°$ in the azimuth direction and a range of $70°$ in the elevation direction. An optical fibre was employed to establish optical connectivity between the spectrometers and the scanner. A fibre core with a diameter of $200\,\mu\mathrm{m}$ was employed for these experiments. Next, we proceeded with two separate measurements to assess the performance of the proposed method. The first experiment in section 4.1 was conducted to enable quantitative evaluation. Additionally, we conducted a second experiment in section 4.2 in a real-world scenario within a Cathedral featuring stained-glass windows.

4.1. Qualitative Evaluation

Two hyperspectral images of a ColorChecker Passport (X-Rite, Inc.) were captured on a partly cloudy afternoon, where the temporal sunlight conditions varied as illustrated

(a) Spectrum Filter
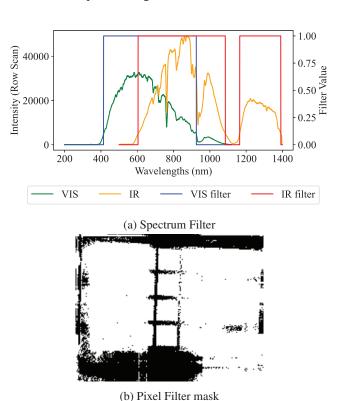

(b) Pixel Filter mask

Figure 6: Overview of filtering, (a) the red and purple lines show the illumination spectrum of the data cube and the green shows the spectral filter, and (b) the white represents pixels that were used while black represents filtered out pixels.

in Figure 3. Specifically, one image ($i^{\rightarrow}$) was obtained through a row-scanning process with a scan time of $1197\,\mathrm{s}$, and the other image was acquired via column-scanning, $i^{\downarrow}$, with a scan time of $1275\,\mathrm{s}$.

We used 3 as the lower limit for the filtering process and the upper limit as 5000. Figure 6 shows the resulting spectrum filter and pixel filter. After filtering, 1351 channels were filtered out. An open-source Python package for colour science [19] synthesised RGB images from the spectral cubes. Figure 7 displays the synthesised RGB images, showcasing the row and column scan images and the outcomes achieved using the RPCA and the proposed method. It is evident from the figure that the images obtained under natural sunlight conditions were significantly influenced by temporal variations in illumination. Conversely, the proposed methods effectively mitigate this variation compared to the RPCA method. Both methods create spatial artefacts, with the proposed method having fewer artefacts than the RPCA method.

The primary objective is to compare the spectra of each colour patch within the compensated spectral cubes $\overline{i_{u,v}}$ against the corresponding spectra in the spectral library. The spectral library introduced by [20] was utilised for this evaluation. This library comprises reflectance values for each colour patch found in the ColorChecker Passport (X-Rite, Inc.). We implemented the pre-processing method stipulated in [11]. In Figure 9, the mean spectra of each colour patch acquired from the row scan and column scan, as well as the compensated cubes generated by both the RPCA method and the proposed method, are presented. These mean spectra are compared to those obtained from the spectral library, which serves as the ground truth reference. It is worth noting that the spectra obtained from both scans differ from those of the library due to the temporal variations in illumination, which impact the estimation of the illumination spectrum. However, the spectra by the proposed method exhibit a much closer resemblance to the groundtruth than the RPCA method. We further evaluated the findings using the RMSE as a quantitative measure. We computed the RMSE between each pixel within the patch and the corresponding ground truth value of the patch across all spectral channels encompassing the spectral library.

Table 1 presents the mean and standard deviation of the root mean square error (RMSE) among different datacubes, and Figure 8 illustrates the relationship between the different datacubes and the RMSE value using a violin plot. As anticipated from the observations in Figure 9, the plot reveals that the proposed method's mean, standard deviation and median RMSE are lower than that of the row scan ($i^{\rightarrow}_{u,v}$), column scan ($i^{\downarrow}_{u,v}$), and RPCA methods. This suggests that, on average, the proposed method achieves better accuracy regarding RMSE. Furthermore, the shape of the violin plot distribution indicates that the RMSE values

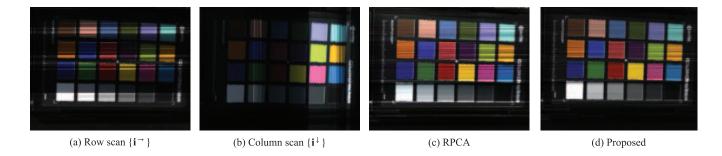| (a) Row scan $\{\mathbf{i}^{\rightarrow}\}$ | (b) Column scan $\{\mathbf{i}^{\downarrow}\}$ | (c) RPCA | (d) Proposed |

Figure 7: RGB images were synthesised from scanned images with illumination variations and mitigated results.

Figure 8: Distribution of RMSE in all the patches.
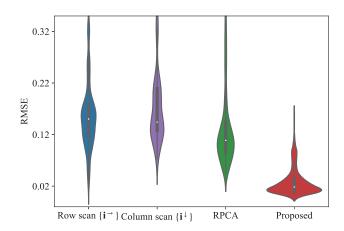
| | Data Cubes | | | |
Metric	$i_{u,v}^{\rightarrow}$	$i_{u,v}^{\downarrow}$	RPCA	Proposed
Mean	0.16	0.19	0.07	0.03
Std	0.07	0.10	0.04	0.02

Table 1: Mean and standard deviation (Std) of the RMSE of the color patches.

of the proposed method are highly concentrated around the median. This implies that the proposed method consistently performs well, as evidenced by the reduced variation in the RMSE values.

4.2. Experiments with Stained- glass windows

Figure 5 shows the experimental setup used to capture hyperspectral images of stained-glass windows inside the *Cathédrale Notre-Dame d'Amiens*, situated in Amiens, France. We captured both row and column scan images for two stained glass windows (**XIII** and **XVIII**) on a partly cloudy day, where the temporal sunlight conditions varied. Table 2 shows the spatial resolution and scan time for the hyperspectral images obtained. We established the lower

| | | | Time for scan (s) | |
ID	Subject	Resolution	Row scan	column scan
(1)	XIII	480×225	4936	5693
(2)	XVIII	520×240	4848	4982

Table 2: Spatial resolution and time consumed for the scans.

limit as 1 for the filtering process and the upper limit as 1000. After filtering, 654 and 716 channels were filtered out for the XIII and XVIII windows, respectively. We then applied the proposed method to the filtered hyperspectral images of the stained-glass windows.

Figures 10 and 11 display the synthesised RGB images along with the mitigated results from the scan. Additionally, to visualise the mitigation effect, we present the difference between the scan and the results obtained through the proposed method in Figure 10 (d) and Figure 11 (d). Compared to the scan, the mitigated result exhibits reduced intensity in the blue regions of the difference image and increased intensity in the red regions.

5. Conclusions

We introduced using a full-column scan to address the challenge of temporal varying illumination in whisk-broom hyperspectral imaging. To solve the problem, we have employed low-dimensional models on the logarithm of reflectance and illumination spectra. Our approach involves using Singular Value Decomposition (SVD) to solve the problem. Experimental results demonstrate that our method can mitigate temporal illumination variations on stained glass windows. Our method can serve in the digital preservation and analysis of stained-glass windows for restoration. In future work, we aim to implement global constraints with improved computational efficiency accounting for the smooth varying of the illumination Spectrum.

Acknowledgement

Figure 9: Comparison of spectra in each colour patch.

(a) Horizontal scan $\{i^{\rightarrow}\}$ (b) Vertical scan $\{i^{\downarrow}\}$ (c) Compensated (d) Diff.
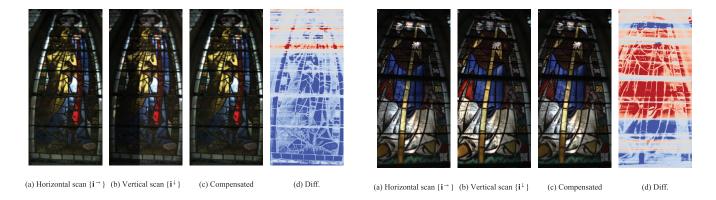
Figure 10: (a–c)Synthesized RGB image of the stained glass window no. XIII, (d) the difference between the row scan ($i^{\rightarrow}$) and the mitigated results.

(a) Horizontal scan $\{i^{\rightarrow}\}$ (b) Vertical scan $\{i^{\downarrow}\}$ (c) Compensated (d) Diff.

Figure 11: (a–c)Synthesized RGB image of the stained glass window no. XVIII, (d) the difference between the row scan ($i^{\rightarrow}$) and the mitigated results.

References

[1] Agnese Babini, Tiziana Lombardo, Katharina Schmidt-Ott, Sony George, and Jon Yngve Hardeberg. Acquisition strategies for in-situ hyperspectral imaging of stained-glass windows: case studies from the Swiss National Museum. *Heritage Science*, 11(1):74, 2023.

[2] David H Brainard and William T Freeman. Bayesian color constancy. *J. Opt. Soc. Am. A*, 14(7):1393–1411, 1997.

[3] G. Buchsbaum. A spatial processor model for object colour perception. *Journal of the Franklin Institute*, 310(1):1–26, 1980.

[4] Po-Rong Chang and Tsung-Hsieh Hsieh. Constrained nonlinear optimization approaches to color-signal separation. *IEEE Transactions on Image Processing*, 4(1):81–94, 1995.

[5] Xiaochuan Chen, Mark S Drew, and Ze-Nian Li. Illumination and reflectance spectra separation of hyperspectral image data under multiple illumination conditions. *IST Electronic Imaging*, 2017(18):194–199, 2017.

[6] Costanza Cucci, John K. Delaney, and Marcello Picollo. Reflectance hyperspectral imaging for investigation of works of art: Old master paintings and illuminated manuscripts. *Accounts of Chemical Research*, 49(10):2070–2079, 2016. PMID: 27677864.

[7] Jan Dariusz Cutajar, Agnese Babini, Hilda Deborah, Jon Yngve Hardeberg, Edith Joseph, and Tine Frøysaker. Hyperspectral Imaging Analyses of Cleaning Tests on Edvard Munch's Monumental Aula Paintings. *Studies in Conservation*, 67(sup1):59–68, 2022.

[8] Mark S. Drew and Graham D. Finlayson. Analytic solution for separating spectra into illumination and surface reflectance components. *Journal of the Optical Society of America (JOSA)*, 24(2):294–303, 2007.

[9] G.D. Finlayson, S.D. Hordley, and P.M. HubeL. Color by correlation: a simple, unifying framework for color constancy. *IEEE Transactions on Pattern Analysis and Machine Intelligence*, 23(11):1209–1221, 2001.

[10] D A Forsyth. A novel algorithm for color constancy. *International Journal of Computer Vision*, 5(1):5–35, 1990.

[11] Takuya Funatomi, Takehiro Ogawa, Kenichiro Tanaka, Hiroyuki Kubo, Guillaume Caron, El Mustapha Mouaddib, Yasuyuki Matsushita, and Yasuhiro Mukaigawa. Eliminating temporal illumination variations in whisk-broom hyperspectral imaging. *International Journal of Computer Vision*, 130(5):1310–1324, 2022.

[12] Liang. Gao and R. Theodore Smith. Optical hyperspectral imaging in microscopy and spectroscopy – a review of data acquisition. *Journal of Biophotonics*, 8(6):441–456, 2015.

[13] Jian Ho, Brian V. Funt, and Mark S. Drew. Separating a color signal into illumination and surface reflectance components: Theory and applications. *IEEE Transactions on Pattern Analysis and Machine Intelligence*, 12:966–977, 1990.

[14] Qian Huang, Weixin Zhu, Yang Zhao, Linsen Chen, Yao Wang, Tao Yue, and Xun Cao. Multispectral image intrinsic decomposition via subspace constraint. In *Proceedings of the IEEE Conference on Computer Vision and Pattern Recognition (CVPR)*, 2018.

[15] Cong Phuoc Huynh and Antonio Robles-Kelly. A Solution of the Dichromatic Model for Multispectral Photometric Invariance. *International Journal of Computer Vision*, 90(1):1–27, 2010.

[16] Deane B. Judd, David L. MacAdam, Günter Wyszecki, H. W. Budde, H. R. Condit, S. T. Henderson, and J. L. Simonds. Spectral distribution of typical daylight as a function of correlated color temperature. *Journal of the Optical Society of America (JOSA)*, 54(8):1031–1040, 1964.

[17] John P. Kerekes and John R. Schott. *Hyperspectral Imaging Systems*, chapter 2, pages 17–45. John Wiley and Sons, Ltd, 2007.

[18] Edwin H Land and John J McCann. Lightness and Retinex Theory. *J. Opt. Soc. Am.*, 61(1):1–11, 1971.

[19] Thomas Mansencal, Michael Mauderer, Michael Parsons, Nick Shaw, Kevin Wheatley, Sean Cooper, Jean D. Vandenberg, Luke Canavan, Katherine Crowson, Ofek Lev, Katrin Leinweber, Shriramana Sharma, Troy James Sobotka, Dominik Moritz, Matt Pppp, Chinmay Rane, Pavithra Eswaramoorthy, John Mertic, Ben Pearlstine, Manuel Leonhardt, Olli Niemitalo, Marek Szymanski, Maximilian Schambach, Sianyi Huang, Mike Wei, Nishant Joywardhan, Omar Wagih, Pawel Redman, Joseph Goldstone, and Stephen Hill. Colour 0.3.16, 2020.

[20] Robin Myers. Spectral library, Chromaxion™, 2020.

[21] Teresa Palomar, Chiara Grazia, Isabel Pombo Cardoso, Marcia Vilarigues, Costanza Miliani, and Aldo Romani. Analysis of chromophores in stained-glass windows using Visible Hyperspectral Imaging in-situ. *Spectrochimica Acta Part A: Molecular and Biomolecular Spectroscopy*, 223:117378, 2019.

[22] Marcello Picollo, Costanza Cucci, Andrea Casini, and Lorenzo Stefani. Hyper-Spectral Imaging Technique in the Cultural Heritage Field: New Possible Scenarios. *Sensors*, 20(10), 2020.

[23] Ruven Pillay, Jon Y Hardeberg, and Sony George. Hyperspectral imaging of art: Acquisition and calibration workflows. *Journal of the American Institute for Conservation*, 58(1-2):3–15, 2019.

[24] Gerrit Polder and Aoife Gowen. The hype in spectral imaging. *Journal of Spectral Imaging*, 9, 2020.

[25] A Yuille. A method for computing spectral reflectance. *Biological Cybernetics*, 56(2):195–201, 1987.

[26] Yinqiang Zheng, Imari Sato, and Yoichi Sato. Illumination and reflectance spectra separation of a hyperspectral image meets low-rank matrix factorization. In *Computer Vision and Pattern Recognition Conference (CVPR)*, pages 1779–1787, 2015.